

# 3 × 3 MIMO Fiber–Wireless System in W-Band with WDM/PDM RoF Transmission Capability

Pham Tien Dat, *Member, IEEE*, François Rottenberg, *Member, IEEE*, Atsushi Kanno, *Member, IEEE*, Naokatsu Yamamoto, Tetsuya Kawanishi, *Fellow, IEEE*

**Abstract**— We propose and demonstrate a 3 × 3 full multiple-input multiple-output (MIMO) fiber–wireless system in the W-band with wavelength-division multiplexing (WDM) and polarization-division multiplexing (PDM) radio-over-fiber (RoF) transmission capability. The system is realized using two highly stable RoF links based on the optical self-heterodyne method and PDM transmission in one of the RoF links. We experimentally demonstrate and confirm satisfactory performances for a 3 × 3 MIMO offset quadrature amplitude modulation-based filter-bank multicarrier signal. Total capacities of approximately 110 and 132 Gb/s, corresponding to spectral efficiencies of approximately 8.5 and 10.2 bits/s/Hz, respectively, are achieved for the system using antennas placed in the same and alternately different polarizations, respectively. The system is applicable to WDM and combined WDM/PDM RoF transmissions. It provides a scalable solution for facilitating large-scale MIMO signal transportation and can be a promising solution for future mobile transport and radio access networks in high-frequency bands.

**Index Terms**— Millimeter-wave, multiple-input multiple-output, seamless fiber–wireless system, radio-over-fiber, mobile fronthaul, fifth-generation and beyond.

## I. INTRODUCTION

SEAMLESS fiber–wireless systems in high-frequency bands, as shown in Fig. 1(a), are considered a reliable and cost-effective solution for mobile transport networks. In this system, wireless links serve as extensions of fiber links for the flexible transmission of mobile signals. In addition, the system can function as a seamless access network to facilitate the deployment of ultra-dense small cells in very high-frequency bands in beyond fifth-generation networks, as shown in Fig. 1(b) [1, 2]. In these systems, high-speed wireless links serve as radio access networks, whereas fiber links function as mobile fronthaul systems. The system is promising for simplifying antenna sites, reducing costs, as well as achieving low power consumption and low latency in ultra-dense small cell networks. In both the abovementioned mentioned use cases, large-scale multiple-input multiple-output (MIMO) fiber–wireless systems are necessitated to increase the transmission capacity and

facilitate the transport of large-scale MIMO radio signals in future mobile networks.

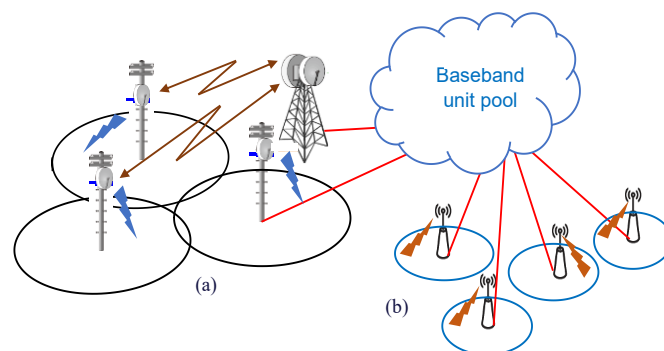


Fig. 1. Use cases of seamless fiber–wireless system: (a) transport links; (b) seamless access network.

Several studies pertaining to MIMO fiber–wireless systems in high-frequency bands have been conducted [3–13]. Wavelength-division multiplexing (WDM) intermediate frequency-over-fiber (IFoF) systems were recently proposed for MIMO radio signal transmission [3–6]. The system is promising owing to its simplicity in the generation of multiple IFoF signals and is scalable for large-scale MIMO signals. However, its antenna site is complicated owing to the use of electrical signal up-conversion. Furthermore, the system is affected by signal-to-signal beat interference and electrical mixers. For applications that require simple antennas, radio-over-fiber (RoF)-based fiber–wireless systems should be considered. Nevertheless, in previous studies [7–12], the size of MIMO signals was limited to 2 × 2 owing to the use of optical polarization-division multiplexing (PDM) RoF systems. Recently, a photonics-aided wireless transmission of 4 × 4 MIMO millimeter-wave signals in the D-band was demonstrated [13]. However, in the system, four wireless links were positioned in parallel; hence, no interference occurred between the radio signals. It is challenging to realize a full MIMO fiber–wireless system for MIMO sizes exceeding 2 × 2 using the optical heterodyne method. This is because the interference between the radio signals, which have rapid and independent fluctuations of the carrier frequency and phase noise, renders the signal synchronization and demodulation

Manuscript received xx, 2021; revised xx, 202x. This work was supported in part by JSPS KAKENHI under Grant 18K04156. (Corresponding author: Pham Tien Dat.)

P. T. Dat, A. Kanno, and N. Yamamoto are with the Network System Research Institute, National Institute of Information and Communication Technology, Tokyo 184-0015, Japan (e-mail: [ptdat@nict.go.jp](mailto:ptdat@nict.go.jp); [kanno@nict.go.jp](mailto:kanno@nict.go.jp); [naokatsu@nict.go.jp](mailto:naokatsu@nict.go.jp)).

F. Rottenberg is with the ICTTEAM Institute, Universite Catholique de Louvain, Louvain-la-Neuve 1348, Belgium (e-mail: [francois.rottenberg@uclouvain.be](mailto:francois.rottenberg@uclouvain.be)).

T. Kawanishi is with the School of Fundamental Science and Engineering, Waseda University, Tokyo 169-8050, Japan (e-mail: [kawanishi@waseda.jp](mailto:kawanishi@waseda.jp)).

Color versions of one or more of the figures in this paper are available online at <http://ieeexplore.ieee.org>.

extremely complicated.

Herein, we propose a  $3 \times 3$  full MIMO fiber–wireless system in the W-band using highly stable RoF technology based on the coherent optical self-heterodyne method. The high carrier frequency stability and low phase noise of each MIMO signal stream render MIMO signal synchronization and demodulation simple. To realize an end-to-end  $3 \times 3$  MIMO signal transmission, we combined two RoF systems with PDM transmission in one of the RoF links. In contrast to previous studies regarding MIMO fiber–wireless systems [7-13], in which emulated PDM MIMO signals were transmitted and demodulated, we demonstrated an end-to-end MIMO signal transmission in this study. Furthermore, we employed a high-spectral-efficiency offset quadrature amplitude modulation-based filter-bank multicarrier (OQAM/FBMC) and adaptive modulation to increase the system capacity. We successfully transmitted approximately 110 and 132-Gb/s of  $3 \times 3$  OQAM/FBMC signals over the system using antennas placed in the same and alternately different polarizations, respectively. This paper is an extended version of our previous conference paper [14, 15]. In this study, we included the details of the experiments and digital signal processing (DSP). Moreover, we evaluated the system performance when all antennas were placed in the same polarization for high-spectral-efficiency MIMO signal transmission. The remainder of this paper is organized as follows. Section II presents the DSP for the MIMO OQAM/FBMC signal. Section III.A presents the experimental setup for a  $3 \times 3$  MIMO fiber–wireless system, and Section III.B presents the experimental results. Finally, Section IV concludes the paper.

## II. DIGITAL SIGNAL PROCESSING

The DSP design is based on our previous study [16]. In the current study, we further optimized the system for  $3 \times 3$  MIMO signal generation and utilized a different noise tracking pre-stream, which enabled a more accurate compensation. In the OQAM signal, complex symbols are first converted to real symbols at a rate that is twice as fast of the complex symbols. The real symbols are alternatively made of the real and imaginary parts of the complex symbols. Therefore, one OQAM symbol can be considered to correspond to two pulse amplitude modulation (PAM) symbols with a time offset. In this study, we allowed an integer number of PAM levels,  $P$ , which is not a power of two, so-called flexible PAM [17]. This mapping is enabled if the bits are mapped to PAM symbols on a block basis. As an example, for a fixed constellation size  $P$ , a group of  $N_b$  bits must be mapped to a group of  $N_d$  PAM symbols. Therefore, we must identify the minimal  $N_d$  such that a one-to-one mapping is achieved. The direct constraint is  $2^{N_b} \leq P^{N_d}$ . By solving this equation, it is discovered that  $\frac{N_b}{\log_2 M} \leq N_d$  and a suitable option is  $N_d = \left\lceil \frac{N_b}{\log_2 P} \right\rceil$ . The efficiency of this mapping is  $\frac{N_b}{N_d \log_2 M} = \frac{N_b}{\log_2 M} / \left\lceil \frac{N_b}{\log_2 P} \right\rceil$ . When  $N_b$  becomes large, the bit mapping loss due to the ceil operator becomes negligible, and the efficiency approaches one. In the system demonstration, we compared the system performance and transmission capacity

using the flexible and standard PAM allocation, which is defined as an integer number of PAM levels with a power of two. For both approaches, we applied adaptive modulation allocations on different subcarriers and signal streams based on the estimated signal-to-noise ratio (SNR) and target error probability. We denote the numbers of subcarriers and complex symbols transmitted on each subcarrier as  $M$  and  $N_s$ , respectively. The set of active subcarriers is denoted by  $\mathcal{M}$ . To simplify analog filtering in our experiment, 5% of the subcarriers at the two edges of the band were set as inactive. Therefore, the bandwidth occupied by the system was  $0.9M/T = 0.9/T_s$ , where  $T$  is the multicarrier symbol period,  $T_s = T/M$  the sampling period, and  $1/T$  the subcarrier spacing. In our experiment, each subcarrier comprised three transmitted streams. However, the system is applicable to any MIMO size. The subscripts  $m$  and  $l$  refer to the subcarrier and multicarrier symbol indexes, respectively. At the transmitter, the bits are first mapped to real PAM symbols  $\mathbf{d}_{m,l} \in \mathbb{R}^{3 \times 1}$  at twice the rate, i.e.,  $2/T$ . The transmit baseband equivalent signal can be written as

$$\mathbf{s}[n] = \sum_{l=0}^{2N_s-1} \sum_{m \in \mathcal{M}} \mathbf{d}_{m,l} g_{m,l}[n],$$

where  $g_{m,l}[n] = j^{m+l} g \left[ n - l \frac{M}{2} \right] e^{j \frac{2\pi m}{M} \left( n - \frac{M\kappa-1}{2} \right)}$ . The pulse  $g[n]$  selected was that of the Phydias prototype filter [18], which is of length  $M\kappa$ , where  $\kappa$  is the overlapping factor. We fixed  $\kappa$  to four in the experiments.

The received signal  $\mathbf{r}[n]$  was processed using an analysis filter bank (AFB). The symbols after the AFB and OQAM compensation are given by

$$\mathbf{z}_{m,l} = \sum_n \mathbf{r}[n] g_{m,l}^*[n]. \quad (1)$$

Typically, in studies pertaining to FBMC, the channel is assumed to be constant over the transmit and receive pulse duration, as well as frequency flat at the subcarrier level. These assumptions hold in our implemented system because the channels are relatively static in time and directive, resulting in few multipath components. Hence, the channels did not change quickly in time and frequency. For extension to a real system, the link would remain directive and therefore relatively stable over time and frequency. Moreover, if the frequency selectivity in the channels is higher, then the number of subcarriers can be adjusted accordingly such that the assumptions can be maintained. Under these assumptions, we can approximate the demodulated symbols  $\mathbf{z}_{m,l}$  as follows:

$$\mathbf{z}_{m,l} \approx \Phi_l \mathbf{H}_m (\mathbf{d}_{m,l} + j\mathbf{u}_{m,l}) + \mathbf{w}_{m,l}, \quad (2)$$

where  $\mathbf{w}_{m,l}$  is the additive noise, and  $j\mathbf{u}_{m,l}$  is the purely imaginary intrinsic interference from neighboring symbols in time and frequency. The MIMO matrix  $\mathbf{H}_m \in \mathbb{C}^{3 \times 3}$  corresponds to the channel frequency response, which is assumed to be static over the frame duration. The matrix  $\Phi_l \in \mathbb{C}^{3 \times 3}$  is a diagonal matrix with the  $i$ -th element being a phasor

equal to  $e^{j\phi_l^{(i)}}$ . The phase  $\phi_l^{(i)}$ , which varies over time and stream but not frequency, represents the effect of phase noise and possible residual carrier frequency offset (CFO) after demodulation. The estimated real symbols  $\hat{\mathbf{d}}_{m,l}$  are obtained based on the real part after channel equalization and phase compensation, i.e.,

$$\hat{\mathbf{d}}_{m,l} = \Re\{\hat{\Phi}_l^* \mathbf{B}_m \mathbf{z}_{m,l}\}. \quad (3)$$

The matrix  $\hat{\Phi}_l$  is the estimate of  $\Phi_l$ , whereas the equalizing matrix  $\mathbf{B}_m$  is fixed based on a linear minimum mean squared error criterion, as follows:

$$\mathbf{B}_m = \left( \hat{\mathbf{H}}_m^H \hat{\mathbf{H}}_m + \frac{\hat{\sigma}_w^2}{\sigma_d^2} I_3 \right)^{-1} \hat{\mathbf{H}}_m^H,$$

where  $\hat{\mathbf{H}}_m$  and  $\sigma_w^2$  are the estimates of  $\mathbf{H}_m$  and the noise variance, respectively, which are obtained during the channel estimation procedure;  $\sigma_d^2$  is twice the variance of the transmitted symbols  $\mathbf{d}_{m,l}$ .

### Preamble structure

A preamble was added to the data symbol frame for channel estimation and synchronization at the receiver. The preamble comprised the 10 first OQAM symbols  $\mathbf{d}_{m,l}$ , which correspond to a duration of  $10T/2 = 5T$ . The preamble was constructed to avoid the effects of intrinsic interference. Therefore, the second, fourth, sixth, and eighth OQAM symbols were only zeros:  $\mathbf{d}_{m,1} = \mathbf{d}_{m,3} = \mathbf{d}_{m,5} = \mathbf{d}_{m,7} = \mathbf{0}, \forall m$ . Furthermore, the ninth and tenth OQAM symbols were zero to protect the preamble from interference due to data symbols. Even subcarriers were filled with pilots, whereas the symbols on the odd subcarriers were all zeros. The even subcarriers of the zeroth OQAM symbol  $\mathbf{d}_{m,0}$  were filled with pseudo-randomly generated  $\pm 1$ , thereby providing a low crest factor in the time domain. For synchronization, the third OQAM symbol was set as a repetition of the first symbol, resulting in  $\mathbf{d}_{m,0} = \mathbf{d}_{m,2}$ . To perform an estimation, the following matrix was created:

$$\mathbf{D}_m = (\mathbf{d}_{m,2} \ \mathbf{d}_{m,4} \ \mathbf{d}_{m,6}) \in \mathbb{C}^{3 \times 3} \text{ if } m \text{ is even and } m \in \mathcal{M}.$$

To estimate the channel,  $\mathbf{D}_m$  must be of full rank. Moreover, for peak-to-average power ratio (PAPR) issues, it is desirable to set  $\mathbf{D}_m = \pm \mathbf{F}_3$ . In fact, the  $3 \times 3$  unitary discrete Fourier transform matrix  $\mathbf{F}_3$  ensures an equal transmit power for each stream, whereas the random  $\pm$  ensures a low PAPR in the time domain.

### Synchronization

The synchronization algorithm utilizes the repetitive patterns of the first and third symbols. This can be regarded as a straightforward extension of the study presented in [19] for the MIMO case. The first step of the algorithm is to detect the start of the frame. This is achieved by maximizing the following detection metric computed based on the AFB outputs of the three receiving antennas, as follows:

$$\xi[l] = \frac{2 \left| \sum_{m \in \mathcal{M}_p} \mathbf{z}_{m,l+2}^H \mathbf{z}_{m,l} \right|}{\sum_{m \in \mathcal{M}_p} (\|\mathbf{z}_{m,l}\|^2 + \|\mathbf{z}_{m,l+2}\|^2)}.$$

Once the beginning of frame  $l$  is detected, the first coarse CFO can be estimated as follows:

$$\epsilon_{CFO} = \frac{1}{2\pi T} \angle \sum_{m \in \mathcal{M}_p} \mathbf{z}_{m,0}^H \mathbf{z}_{m,2}, \quad (4)$$

where the first OQAM symbol corresponds to the first demodulated symbol of the frame. Based on the coarse CFO estimate, the CFO can be corrected in the time domain before performing a second AFB demodulation. Subsequently, the CFO is re-estimated using Equation (4). Next, the symbol timing offset (STO) is estimated as

$$\tau_{STO} = \frac{T}{4\pi} \angle \sum_{i=\{1,2,3\}} \sum_{l=\{0,2\}} \sum_{\{m,m+2\} \in \mathcal{M}_p} \frac{z_{m+2,l}^{(i)*} z_{m,l}^{(i)}}{z_{m+2,l}^{(i)} z_{m,l}^{(i)}}.$$

The remainder of the frame is demodulated using the refined CFO and STO estimates.

### Channel and noise variance estimation

Channel estimation relies on the transmission of the second, fourth, and, sixth OQAM symbols. We can define the matrix of demodulated symbols at each subcarrier for the three streams and three OQAM symbols of interest as follows:

$$\mathbf{Z}_m = (\mathbf{z}_{m,2} \ \mathbf{z}_{m,4} \ \mathbf{z}_{m,6}) \in \mathbb{C}^{3 \times 3}.$$

Using the fact that, at the pilot positions, the intrinsic interference is negligible owing to the neighboring guard symbols ( $\mathbf{u}_{m,l} \approx \mathbf{0}$ ), the demodulated symbols  $\pm \mathbf{F}_3$  can be correlated with the transmitted pilot symbols as

$$\mathbf{Z}_m = \mathbf{H}_m \mathbf{D}_m + \mathbf{W}_m,$$

where  $\mathbf{W}_m \in \mathbb{C}^{3 \times 3}$  is the matrix of the noise samples. Subsequently, the least-squares estimate of  $\mathbf{H}_m$  at the pilot positions can be estimated as

$$\hat{\mathbf{H}}_m = \mathbf{Z}_m \mathbf{D}_m^{-1} = \mathbf{H}_m + \mathbf{W}_m \mathbf{D}_m^{-1}.$$

However, the channel frequency response is only known at the pilot positions, and the response at the non-pilot subcarriers should be interpolated. In practice, the channel impulse response contains only a finite number of significant taps, such that  $L \ll M$ . This knowledge can be used to obtain the average of the noise effect and to interpolate the channel [20]. Details regarding the specific time-domain method used in this study, which was straightforwardly extended to the MIMO case, are available in [21]. Moreover, based on the residual error between  $\hat{\mathbf{H}}_m$  and the interpolated channel, the noise variance  $\sigma_w^2$  can be estimated.

### Phase tracking

The demodulated symbols can be affected by the phase rotation, which must be compensated to avoid phase drifts. To track phase  $\phi_l^{(i)}$ , we used the maximum likelihood phase estimator derived in [21]. It was independently applied on a stream basis. The algorithm proposed in [22] is low in complexity and decision directed, thereby obviating the insertion of pilots in the data frame and avoiding a decrease in spectral efficiency. The phase at OQAM symbol  $l$  and for stream  $i$  can be estimated as follows:

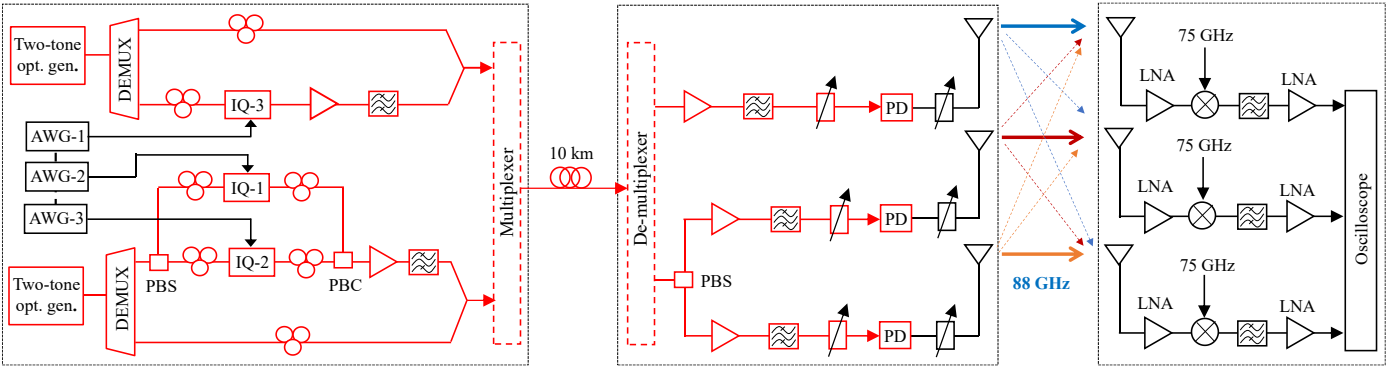


Fig. 2. Experimental setup for  $3 \times 3$  MIMO seamless fiber-wireless system in W-band. Dashed line parts signify emulation of real WDM RoF system and were not implemented.

$$\hat{\phi}_l^{(i)} = \hat{\phi}_{l-1}^{(i)} + \frac{\left(\frac{\sigma_w^2}{\sigma_d^2} + 1\right) \sum_{m \in \mathcal{M}_p} \tilde{z}_{m,l}^{I,(i)} d_{m,l}^{(i)} - \sum_{m \in \mathcal{M}_p} \tilde{z}_{m,l}^{R,(i)} \tilde{z}_{m,l}^{I,(i)}}{\sum_{m \in \mathcal{M}_p} (\tilde{z}_{m,l}^{I,(i)})^2},$$

where  $\tilde{z}_{m,l}^{R,(i)}$  and  $\tilde{z}_{m,l}^{I,(i)}$  are the real and imaginary parts of the demodulated symbols after channel equalization and phase compensation based on the previous estimate, respectively, i.e., the  $i$ -th element of vectors  $\tilde{\mathbf{z}}_{m,l}^R = \Re(\hat{\Phi}_{l-1}^* \mathbf{B}_m \mathbf{z}_{m,l})$  and  $\tilde{\mathbf{z}}_{m,l}^I = \Im(\hat{\Phi}_{l-1}^* \mathbf{B}_m \mathbf{z}_{m,l})$ , respectively. The estimated transmitted symbols  $d_{m,l}^{(i)}$  are obtained by the direct detection of symbols  $\tilde{z}_{m,l}^{R,(i)}$ .

#### Bit loading

After channel and noise variance estimation are performed by the receiver, the SNR is estimated at each subcarrier  $m$  and stream  $i$ . By definition,  $SNR_{m,i} = NMSE_{m,i}^{-1}$ . Here,  $NMSE_{m,i} = [NMSE_m]_{i,i}$  and

$$\begin{aligned} NMSE_m &= \frac{2}{\sigma_d^2} E \left[ (\mathbf{d}_{m,l} - \hat{\mathbf{d}}_{m,l})(\mathbf{d}_{m,l} - \hat{\mathbf{d}}_{m,l})^H \right] \\ &= \frac{2}{\sigma_d^2} E \left[ (\mathbf{d}_{m,l} - \Re\{e^{-j\phi_l} \mathbf{B}_m \mathbf{z}_{m,l}\})(\mathbf{d}_{m,l} - \Re\{e^{-j\phi_l} \mathbf{B}_m \mathbf{z}_{m,l}\})^H \right] \\ &= (\mathbf{B}_m \mathbf{H}_m - \mathbf{I}_3)(\mathbf{B}_m \mathbf{H}_m - \mathbf{I}_3)^H + \frac{\sigma_w^2}{\sigma_d^2} \mathbf{B}_m \mathbf{B}_m^H, \end{aligned}$$

where we used the expression of  $\hat{\mathbf{d}}_{m,l}$  in (3) and the approximation of  $\mathbf{z}_{m,l}$  in (2) [23]. Additionally, we assumed that the phase noise and MIMO channel were perfectly estimated. Based on the channel and noise variance estimates, the related equalization matrices  $\mathbf{B}_m$ ,  $SNR_{m,i}$  can be estimated for each subcarrier and stream.

For a specified SNR value, the PAM constellation level  $M_{m,i}$  of the transmitted symbols (not pilots) assigned to subcarrier  $m$  and stream  $i$  can be fixed such that the target bit error rate  $BER_{m,i}^{target}$  is maintained. The relation between  $BER_{m,i}^{target}$  and  $M_{m,i}$  for a specified  $SNR_{m,i}$  is written as

$$BER_{m,i}^{target} \geq \frac{1}{\log_2(M_{m,i})} \frac{M_{m,i} - 1}{M_{m,i}} \operatorname{erfc} \left( \sqrt{\frac{3SNR_{m,i}}{2(M_{m,i}^2 - 1)}} \right).$$

It is noteworthy that  $M_{m,i}$  is the PAM constellation level of symbols  $d_{m,l}^{(i)}$ . Notably, although we changed the modulation level for each stream and subcarrier, no power loading was used. After bit loading, the modulation levels differed for the different subcarriers and streams; however, the remainder of the FBMC/OQAM transceiver chain remained the same, including operations all signal processing previously described, i.e., the preamble design, synchronization, equalization, channel estimation, and phase tracking.

### III. $3 \times 3$ MIMO FIBER-WIRELESS SYSTEM DEMONSTRATION

#### A. Experimental Setup

The experimental setup for the  $3 \times 3$  MIMO fiber-wireless seamless system in the W-band is shown in Fig. 2. To realize an end-to-end  $3 \times 3$  MIMO signal transmission, a system using three WDM RoF channels can be employed for signal generation and transmission over the optical link. However, owing to the availability of two-tone optical signal generators in our laboratory, we used two RoF links and a PDM transmission in one of the RoF links for the  $3 \times 3$  MIMO signal transmission. In addition, because the two-tone optical signal generators used in the experiment operate at the same wavelength, we generated RoF signals at the same wavelength and transmitted them to the antenna site using different single-mode fibers (SMFs) (not shown in Fig. 2). Nevertheless, the system concept used in this study can be easily applied to actual WDM RoF transmissions. In this case, WDM RoF signal multiplexing and demultiplexing (shown by the dashed lines in Fig. 2) should be implemented before and after fiber transmission using optical couplers and optical filters/wave-shapers, respectively.

In our experiment, two optical millimeter-wave signals with a frequency separation of 79.6 GHz were generated using two-tone optical signal generators. The generators can generate stable coherent two-sideband signals using high-precision optical modulation technology [24, 25]. Similar to single-input single-output (SISO) RoF systems [26], in each RoF channel, optical sidebands from each two-tone optical signal generator were separated using an arrayed waveguide grating. One of the sidebands was modulated by one of the MIMO OQAM/FBMC signal streams. To reduce the effects of fiber dispersion, optical single-sideband signals were generated using in-

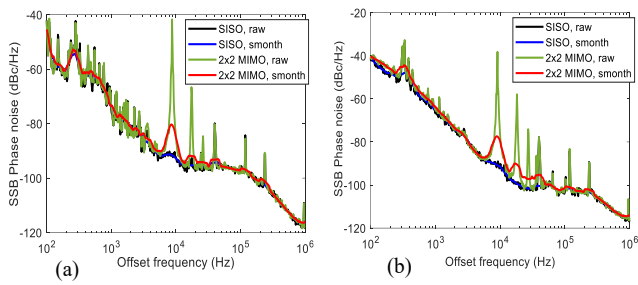


Fig. 3 Phase noise characteristics of SISO and  $2 \times 2$  MIMO system using two RoF links: (a) phase noise of channel 1; (b) phase noise of channel 2.

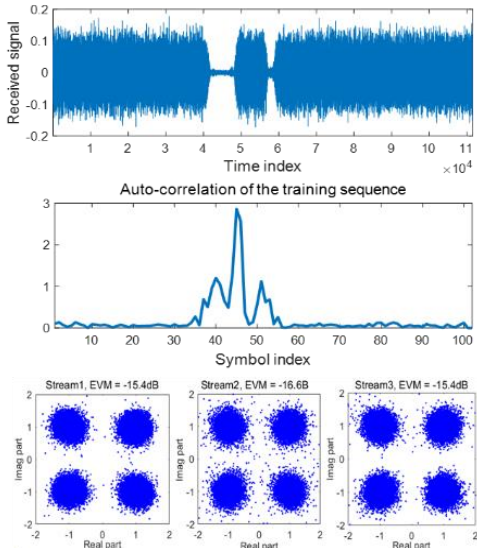


Fig. 4. Received signal of training signals.

phase/quadrature (IQ) optical modulators and by adjusting the bias voltage of the modulators. The other sideband remained unmodulated to function as a reference signal for signal up-conversion at the antenna site. The modulated optical signals were combined with unmodulated sidebands using 3-dB optical couplers, and the combined signals were transmitted to the antenna site using 10-km SMFs. For the PDM RoF link, the transmission was similar to those of other optical PDM systems [7]. One of the optical sidebands of the RoF signal was separated using a polarization beam splitter (PBS). The separated optical polarizations from the PBS were modulated by two different MIMO signal streams. Optical polarization controllers (PCs) were utilized to align the modulated signals to the x- and y-axis polarization components. The modulated optical signals were combined using a polarization beam combiner (PBC), amplified using an optical amplifier, and consequently combined with the unmodulated optical sideband whose polarization was set at  $45^\circ$  from the x-axis using a PC. At the receiver, another PBS was used to split the x- and y-axis-aligned polarization RoF components. The received RoF signals were amplified using optical amplifiers and filtered to suppress the amplified spontaneous emission noise before being input to high-speed photomixers. The generated radio signals at 87.6 GHz, which were formed by 79.6 GHz-spaced two-tone optical signals and optical single-sideband modulation at one of the sidebands, were emitted into free space using a set of three

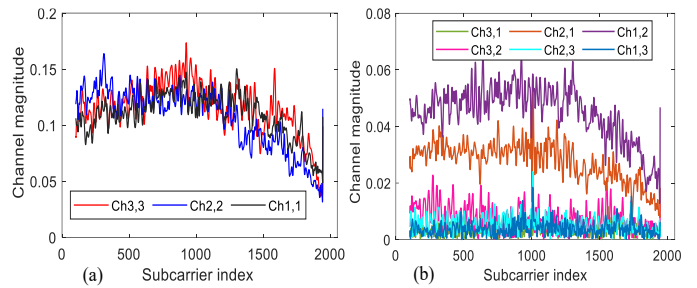


Fig. 5 Channel magnitude of system using antennas placed in different polarizations: (a) main channels; (b) channel response due to interferences.

23-dBi (3-dB beamwidth of  $9^\circ$ ) horn antennas. After a transmission over approximately 1 m in free space, the signals were received by another set of three 23-dBi horn antennas. The adjacent antenna pairs were spaced approximately 10 cm apart. The abovementioned distance was selected owing to the space required to place adjacent receivers in our setup. This arrangement guarantees interferences between the MIMO radio signals when all antenna pairs are placed in the same polarization because the beam coverage of each signal stream at the receiver is approximately 15.7 cm. To evaluate the system performance with and without the presence of cross-interference in the wireless links, we placed the antennas in the same and alternately different polarizations. The received signals were amplified using low-noise amplifiers and down-converted to the intermediate frequency band at 12.5 GHz using electrical mixers. The signals were amplified, sent to a real-time oscilloscope, and finally demodulated offline.

To demonstrate an end-to-end MIMO signal transmission over the system, we generated a  $3 \times 3$  MIMO OQAM/FBMC signal in MATLAB and downloaded it to three synchronized arbitrary waveform generators (AWGs). The signals had a bandwidth of 13 GHz and were modulated around an intermediate frequency of 8 GHz. The number of subcarriers was fixed at 2048, of which 102 subcarriers on each edge of the spectrum were set as inactive to simplify the digital-to-analog conversion. The real-valued intermediate frequency signals from the AWGs were input to  $90^\circ$  hybrid couplers to separate them into two parts with a phase difference of  $90^\circ$  before being input to the IQ optical modulators. It is well acknowledged that the channel response and SNRs of the received signals vary with different subcarriers and signal streams owing to the non-flat frequency response of signal generators as well as optical and electrical devices. Hence, in this study, we adopted an adaptive modulation scheme to effectively exploit the non-uniform channel response of the system. Details regarding the MIMO OQAM/FBMC signal generation and demodulation are presented in the previous section.

### B. Experimental Results

In previous MIMO fiber-wireless systems [7-13], RoF systems based on PDM transmission were employed, where PDM RoF signals are generated from the same light-wave source. Consequently, the frequency fluctuations of MIMO radio signals are identical, thereby enabling a simple optical heterodyne method using free-running lasers to be employed for MIMO signal transmission. However, for large-scale

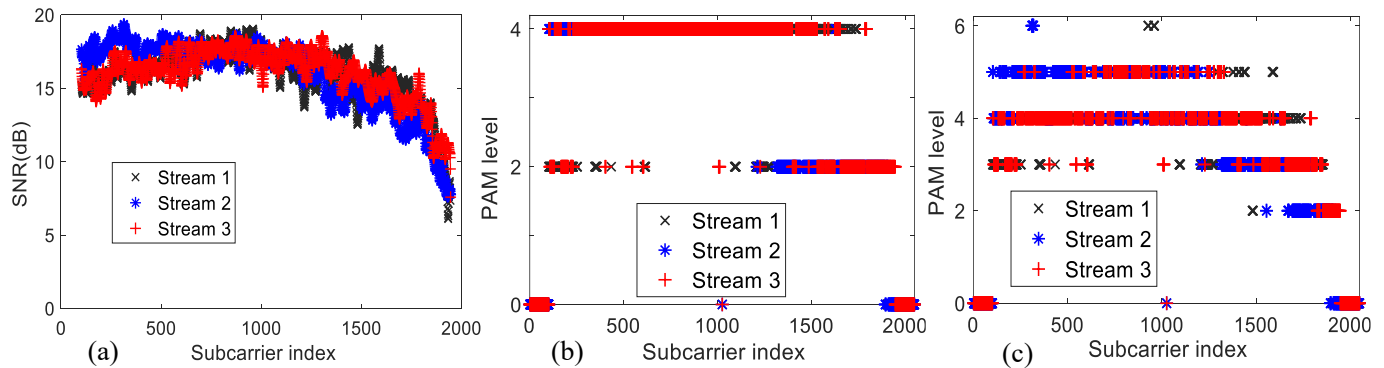


Fig. 6 System using antennas placed in different polarizations: (a) Estimated single-to-noise ratios; (b) estimated standard PAM levels; (c) estimated flexible PAM levels.

MIMO fiber-wireless systems, the use of WDM RoF transmission is indispensable. In these systems, the generation of frequency-stable and low-phase-noise radio signals is crucial for attaining high performances and reducing the complexity of the DSP at the receiver. This is because the interference between the wireless signals, which are generated from different light-wave sources, renders the estimation of carrier frequency offset as well as the phase tracking and demodulation of the signal extremely challenging. In our system, we employed frequency stable and low-phase-noise RoF systems based on the self-optical heterodyne method; hence, the frequency fluctuation and phase noise in each MIMO signal stream are relatively low.

We measured the phase noise characteristics of the received carrier signals of the SISO and MIMO fiber-wireless systems. In this measurement, to include interference between MIMO signals, we placed all antenna pairs in the same polarization. To investigate the interference effect of radio signals generated from different light sources, we turned off one of the PDM RoF channels and measured the performances of a SISO and a  $2 \times 2$  MIMO system using two different RoF links. Only the carrier signal at 8 GHz was transmitted for this measurement. Figs. 3(a) and (b) show the single-sideband phase noise characteristics of the signals in channel 1 and channel 2 of the  $2 \times 2$  MIMO system, respectively. The SISO system was measured by obstructing the signal from the other MIMO streams. Using precision optical modulation technology-based two-tone optical signal generators, which could generate highly stable radio signals [25], low-phase-noise radio signals could be generated in each MIMO signal stream. As shown in the figures, the phase noise of the generated radio signals is much lower than those of the signal generated using optical heterodyne method, even with the use of an optical phase locked loop [27]. Consequently, the phase noise of the MIMO signals was relatively small, even with added interference from the other signal stream.

We subsequently evaluated the performance of the  $3 \times 3$  MIMO fiber-wireless system based on two cases: (1) adjacent antenna pairs placed alternately in different polarizations for negligible interference in the wireless links, and (2) all antennas placed in the same polarization for significant interference between signals. We first investigated the performance for the first case. Initially, a training signal was

transmitted to estimate the SNRs and respective modulation levels for different subcarriers on each signal stream. Figure 4 shows an example of the received training signals in the time domain and its autocorrelation and constellations. Complex OQAM constellations were obtained for stream  $i$  by plotting  $\hat{d}_{m,2l}^{(i)} + j\hat{d}_{m,2l+1}^{(i)}$ , where  $\hat{d}_{m,l}^{(i)}$  is the  $i$ -th element of  $\hat{\mathbf{d}}_{m,l}$  obtained using (3). Clear constellations were observed when an equal 4-OQAM signal (corresponding to 2-PAM symbols  $\hat{d}_{m,l}^{(i)}$ ) was applied for all the subcarriers and signal streams. Subsequently, we measured the channel response of the main channels and interference from the other channels, as shown in Fig. 5. A non-flat channel response was clearly observed in all channels. The significant amplitude reduction in the high-frequency region was due to the low-pass-filter-like response of the AWGs used in the experiment. In the experiment, AWGs with a sampling rate of 50 Gs/s and a bandwidth of 15 GHz were used. Furthermore, interference was observed between signal streams 1 and 2, as shown by the Ch1,2 and Ch2,1 curves in Fig. 5(b). This is caused by optical polarization crosstalk between the PDM RoF signals, which were transmitted over the same RoF link. Notably, in the experiment, the polarization controllers in the PDM RoF links were not fully optimized; therefore, the polarization crosstalk between the channels was not fully minimized. The interference between signal streams 1 and 3 as well as between signal streams 2 and 3 was negligible as these signals were transmitted over different RoF links. The interference in the wireless links was negligible because the adjacent antenna pairs were placed alternately in different polarizations. The estimated SNRs for the different active subcarriers in different signal streams are shown in Fig. 6(a). The estimated modulation levels using standard and flexible PAMs are shown in Figs. 6(b) and (c), respectively. The estimated values for both the active and inactive subcarriers are shown in these figures. As mentioned above, to simplify the digital-to-analog conversion, 102 subcarriers on each edge of the spectrum and subcarrier #1024 (DC channel) were set to be inactive. This is shown by the estimated number of zero-bits in the figures. It is noteworthy that the estimated SNR values for the inactive subcarriers are not shown in Fig. 6(a).

Consequently, we applied different modulation levels on different subcarriers and signal streams, and then transmitted

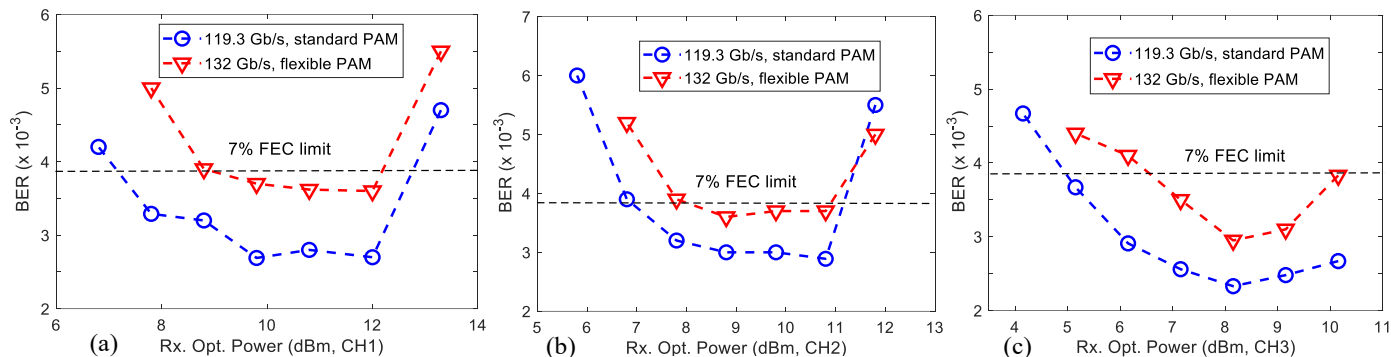


Fig. 7. BER performance of 3 × 3 MIMO FBMC signal of system using RF antennas placed alternately in different polarizations vs. (a) received optical powers in channel 1, (b) received optical powers in channel 2, and (c) received optical powers in channel 3.

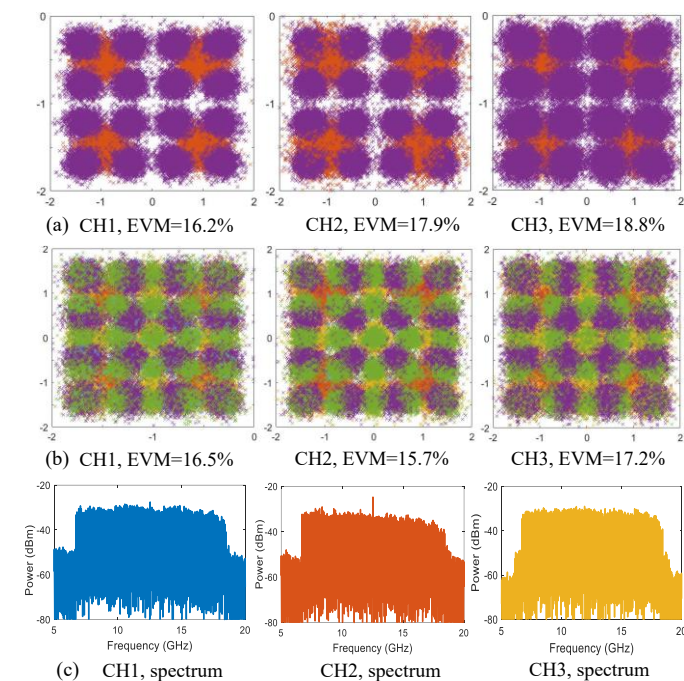


Fig. 8. Examples of constellations and spectrums of received signals in different streams: (a) constellations using standard PAM; (b) constellations using flexible PAM; (c) received spectra.

the signals over the system. The total capacity was calculated by summing the number of bits applied to all the subcarriers and signal streams. It is noteworthy that although we changed the modulation level for the subcarriers on each channel, the symbol variance remained the same. The remainder of the OQAM/FBMC transceiver chain was the same as the case of fixed modulation, including the preamble design, synchronization, equalization, channel estimation, and phase tracking. The performances of the signals after they were transmitted over the system for different received optical powers in each channel are shown in Fig. 7. Total capacities of 119.3 and 132 Gb/s, corresponding to spectral efficiencies of approximately 9.2 and 10.2 bits/s/Hz, respectively, were obtained using standard and flexible PAM modulation, respectively. Applying a flexible PAM can yield a higher data transmission capacity but at the expense of a higher bit error rate (BER). This is because in a flexible PAM, the PAM levels assigned to the subcarriers can be larger than those using

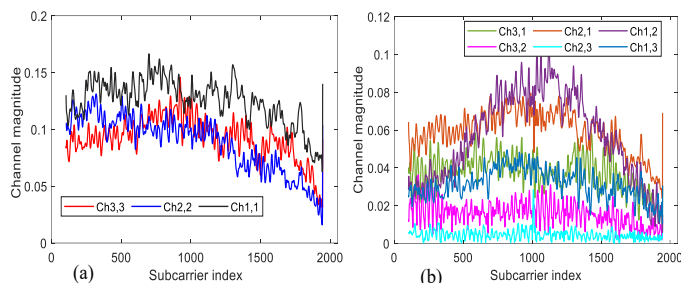


Fig. 9 Channel magnitude of system using antennas placed in same polarization: (a) main channels; (b) channel response due to interference.

standard PAM (as shown in Figs. 6(b) and (c)), thereby resulting in a higher BER, since the SNRs for the two cases are identical. Examples of OQAM constellations using standard PAM, flexible PAM, and the received spectra of the MIMO signals are shown in Figs. 8(a), (b), and (c), respectively. All the transmissions can satisfy a 7% forward error correction (FEC) limit BER of  $3.8 \times 10^{-3}$ . Notably, compared with previous MIMO fiber–wireless systems [10–13], the capacity obtained in this study was lower. Nevertheless, we focused on the feasibility study of a large-scale and flexible end-to-end MIMO fiber–wireless system, which has not been reported to date. Several approaches can be used to further increase the capacity of the system. In our experiment, we used single-output AWGs to generate real-valued intermediate frequency signals, and the signal quality degraded in the high-frequency region owing to the limited analog bandwidth. We expect an increase in the system performance and capacity when using high-performance AWGs and/or multiple AWGs to generate high-quality complex baseband signals for optical modulation. In addition, the primary objective of this study was to use MIMO multiplexing technology to enhance the system capacity. In a practical system, MIMO multiplexing can be combined with a diversity method to increase the transmission distance and/or reduce the outage probability.

For large-scale MIMO systems, it is difficult to avoid interference between the wireless links because the antennas should be placed close to each other. In addition, for high-spectral-efficiency full-duplex transmission, PDM technology should be utilized in wireless links for signal transmission in different directions. In this case, antennas with the same polarization should be placed for signal transmission in one

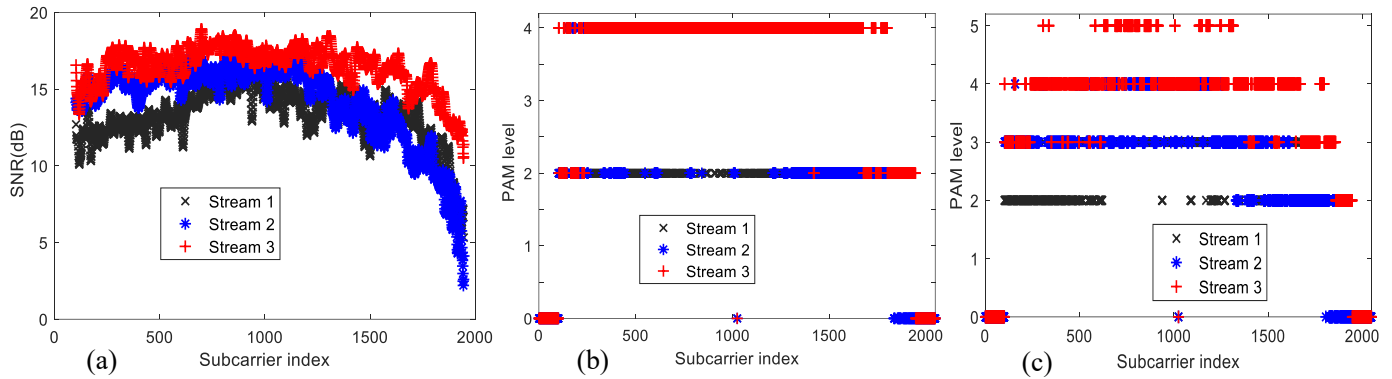


Fig. 10. System using antennas placed in same polarization: (a) estimated single-to-noise ratios; (b) estimated standard PAM levels; (c) estimated flexible PAM levels.

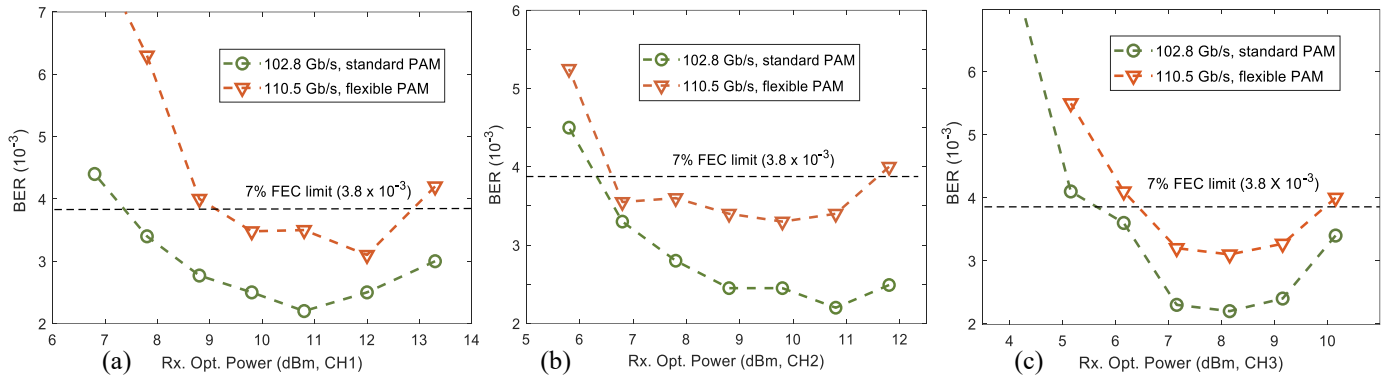


Fig. 11. BER performance of  $3 \times 3$  MIMO FBMC signal of system using RF antennas placed in same polarization vs. (a) received optical powers in channel 1, (b) received optical powers in channel 2, and (c) received optical powers in channel 3.

direction. Nevertheless, strong interference between the signals can complicate signal processing and degrade performance. We evaluated the proposed system under this condition by placing all antennas in the same polarization. Similar to the first case, we first transmitted a training signal and measured the channel response and interference between the signal streams. The results are shown in Figs. 9(a) and (b), respectively. It is clearly observed that, compared with the system in which antennas are alternately placed in different polarizations, interference between the signal streams increased significantly, particularly between streams 1 and 2 as well as streams 1 and 3, as indicated by the Ch1,2 and Ch2,1 as well as Ch1,3 and Ch3,1 curves in Fig. 9(b), respectively. However, the interference between streams 2 and 3 (shown by Ch2,3 and Ch3,2 curves in Fig. 9(b)) was maintained at a low level. This is because, in the experiment, we placed the antennas of channel 1 between those of channels 2 and 3. The strong interference between streams 1 and 2 was also induced by polarization crosstalk in the optical links, similar to the first case. Subsequently, we estimated the SNRs for different subcarriers in different signal streams. The results, as shown in Fig. 10(a), indicate that they are smaller than those of the system using antennas placed alternately in different polarizations owing to the increase in interference. Subsequently, the bit loading levels were calculated based on the received SNRs. The results for the cases where standard and flexible PAMs were applied are shown in Figs. 10(b) and (c), respectively. Owing to the increased signal interferences between the signal streams in the wireless links, the total

capacity was reduced to approximately 102.8 and 110.5 Gb/s, corresponding to spectral efficiencies of approximately 7.9 and 8.5 bits/s/Hz, respectively, using standard and flexible PAM, respectively. The performance of the system when the estimated modulation was applied for different received optical powers in different RoF links is shown in Fig. 11. In this measurement, we fixed the powers on the other channels while changing the power in one channel. In the low-power regions, the performance of the channel, hence, the performance of the entire system deteriorated owing to an insufficient SNR. In the high-power regions, the system performance was affected by both nonlinear distortions in the channel as well as increasing interference in the other channels. Nevertheless, all the transmissions satisfied the 7% FEC overhead BER limit of  $3.8 \times 10^{-3}$ .

Notably, the MIMO signal performance was relatively sensitive to the fiber delay difference between the signal streams. To successfully demodulate the MIMO signal, a delay difference of less than a symbol period should be maintained between the signal streams. In the experiment, we optimized the delay difference between the channels by adding different fibers to the RoF channels. When applied to a real WDM RoF system, MIMO signal synchronization can be affected by the different chromatic dispersions experienced by the different signal streams. In addition, multiplexing and demultiplexing RoF signals can cause additional delays between the signal streams. However, the delay differentials between the signal streams can be compensated by inserting delay fibers into the

optical channels. The delays can also be compensated by DSP at the receiver or transmitter. Because the delay difference between the channels can be estimated in the system calibration, appropriate delays can be added to the signals to equalize them before transmitting or demodulating the signals. Furthermore, other multichannel fiber options, such as multicore and few-mode fibers and their combination with traditional WDM/PDM transmission, would be promising for supporting large-scale MIMO signal transmission in future mobile networks [28, 29].

#### IV. CONCLUSION

In this study, the first  $3 \times 3$  full MIMO fiber-wireless seamless system in the W-band using high-spectral-efficiency and adaptive OQAM/FBMC modulation was demonstrated. Using a highly stable RoF system based on the coherent optical self-heterodyne method, we could utilize different RoF links for large-scale MIMO signal transmission. Satisfactory performance was confirmed experimentally for a  $3 \times 3$  end-to-end MIMO signal transmission with total capacities of 110 and 132 Gb/s and the BER under 7% FEC limit for a system using antennas with the same and alternately different polarizations, respectively. The system is scalable for large MIMO signal transmission by adding WDM and/or PDM RoF channels. The proposed system is promising for high-capacity fiber-wireless transport systems and/or large-scale MIMO radio access signals in high-frequency bands.

#### REFERENCES

- [1] J. Lee et al., "Spectrum for 5G: Global Status, Challenges, and Enabling Technologies," *IEEE Communication Magazine*, Vol. 56, Iss. 3, pp. 12-18, March 2018.
- [2] Y. W. Chen et al., "Key Enabling Technologies for the Post-5G Era: Fully Adaptive, All-Spectra Coordinated Radio Access Network with Function Decoupling," *IEEE Communications Magazine*, Vol. 58, No. 9, pp. 60-66, Oct. 2020.
- [3] J. Kim et al., "MIMO-Supporting Radio-Over-Fiber System and its Application in mmWave-Based Indoor 5G Mobile Network," *Journal of Lightwave Technology*, Vol. 38, No. 1, pp 101 – 111, Jan. 2020.
- [4] E. Ruggeri et al., "A 5G Fiber Wireless 4Gb/s WDM Fronthaul for Flexible 360 Coverage in V-Band massive MIMO Small Cells," *Journal of Lightwave Technology*, Early Access, 2020.
- [5] U. Habib et al., "Single Radio-Over-Fiber Link and RF Chain-Based 60 GHz Multi-Beam Transmission," *Journal of Lightwave Technology*, Vol. 37, No. 9, pp. 1974- 1980, May 2019.
- [6] P. T. Dat et al., "High-Speed Radio-on-Free-Space Optical Mobile Fronthaul System for Ultra-Dense Radio Access Network," in *Proc. OFC 2020, W2A.37*.
- [7] A. Kanno et al., "Optical and millimeter-wave radio seamless MIMO transmission based on a radio over fiber technology," *Optics Express*, Vol. 20, Iss. 28, pp. 29395-29403, 2012.
- [8] X. Pang et al., "100 Gbit/s hybrid optical fiber-wireless link in the W-band (75–110 GHz)," *Optics Express*, Vol. 19, No. 25, pp. 24944-24949, Dec. 2011.
- [9] J. Zhang et al., "Multichannel 120-Gb/s Data Transmission Over  $2 \times 2$  MIMO Fiber-Wireless Link at W-Band," *IEEE Photonics Technology Letters*, VOL. 25, NO. 8, April. 2013.
- [10] R. Puerta et al., "Single-Carrier Dual-Polarization 328-Gb/s Wireless Transmission in a D-Band Millimeter Wave  $2 \times 2$  MU-MIMO Radio-Over-Fiber System," *Journal of Lightwave Technology*, Vol. 36, No. 2, pp. 587 – 593, Jan. 2018.
- [11] S. Jia et al., " $2 \times 300$  Gbit/s Line Rate PS-64QAM-OFDM THz Photonic-Wireless Transmission," *Journal of Lightwave Technology*, Vol. 38, No. 17, pp. 4715 – 4721, 2020.
- [12] J. Yu et al., "432-Gb/s PDM-16QAM Signal Wireless Delivery at W-band using Optical and Antenna Polarization Multiplexing," in *Proc. ECOC 2014, We.3.6.6*.
- [13] X. Li et al., "1-Tb/s Millimeter-Wave Signal Wireless Delivery at D-Band," *Journal of Lightwave Technology*, Vol. 37, No. 1, pp. 196 – 204, Jan. 2019.
- [14] P. T. Dat et al., "101 Gb/s  $2 \times 2$  End-to-End MIMO Fiber-Wireless System in W Band Using WDM Radio-over-Fiber," *Proc. IEEE MWP 2020*, Nov. 2020.
- [15] P. T. Dat et al., "132 Gb/s  $3 \times 3$  Full MIMO Fiber-Wireless Seamless System in W Band Using WDM/PDM RoF Transmission," *Proc. ECOC 2020*, Dec. 2020.
- [16] F. Rottenberg et al., " $2 \times 2$  MIMO FBMC-OQAM Signal Transmission over a Seamless Fiber-Wireless System in W-band," *IEEE Photonic Journal*, Vol. 10, No. 2, pp. 1-14, 2018.
- [17] X. Zhou et al., "Beyond 1 Tb/s Intra-Data Center Interconnect Technology: IM-DD OR Coherent?" *Journal of Lightwave Technology*, Vol. 38, No. 2, pp. 475 – 484, 2019.
- [18] M. G. Bellanger, "Specification and design of a prototype filter for filter bank based multicarrier transmission," in *IEEE International Conference on Acoustics, Speech, and Signal Processing*, 2001, pp. 2417-2420.
- [19] C. Thein et al., "Analysis of frequency domain frame detection and synchronization in OQAM-OFDM systems," *EURASIP Journal on Advances in Signal Processing*, vol. 2014, no. 1, p. 83, Jun. 2014. [Online]. Available: <https://doi.org/10.1186/1687-6180-2014-83>
- [20] M. K. Ozdemir et al., "Channel estimation for wireless OFDM systems," *IEEE Communications Surveys Tutorials*, vol. 9, no. 2, pp. 18-48, Second 2007.
- [21] F. Rottenberg et al., "Generalized optimal pilot allocation for channel estimation in multicarrier systems," in *2016 IEEE 17th International Workshop on Signal Processing Advances in Wireless Communications (SPAWC)*, July 2016, pp. 1-5.
- [22] F. Rottenberg et al., "ML and MAP phase noise estimators for optical fiber FBMC-OQAM systems," in *2017 IEEE International Conference on Communications (ICC)*, May 2017, pp. 1-6.
- [23] F. Rottenberg et al., "Single-tap precoders and decoders for multiuser MIMO FBMC-OQAM under strong channel frequency selectivity," *IEEE transactions on signal processing*, vol. 65, no. 3, pp. 587-600, 2016.
- [24] A. Kanno et al., "Coherent Radio-over-Fiber and Millimeter-wave Radio Seamless Transmission System for Resilient Access Networks" *IEEE Photonics Journal*, Vol. 4, No. 6, Dec. 2012.
- [25] Kanno et al., "Evaluation of Frequency Fluctuation in Fiber-Wireless Link with Direct IQ Down-Converter," *Proc. ECOC 2014, Cannes – France, We.3.6.3*.
- [26] P. T. Dat et al., "Seamless Convergence of Fiber and Wireless Systems for 5G and Beyond Networks," *Journal of Lightwave Technology*, Vol. 37, No. 2, pp. 592 – 605, Jan. 2019.
- [27] S. Rommel et al., "Towards a Scaleable 5G Fronthaul: Analog Radio-over-Fiber and Space Division Multiplexing," *Journal of Lightwave Technology*, Vol. 38, No. 19, pp. 5412 - 5422, 2020.
- [28] A. Macho et al., "Next-Generation Optical Fronthaul Systems Using Multicore Fiber Media," *Journal of Lightwave Technology*, Vol. 34, No. 20, pp. 4819 – 4827, 2016.
- [29] S. Rommel et al., "High-Capacity 5G Fronthaul Networks Based on Optical Space Division Multiplexing," *IEEE Transactions on Broadcasting*, Vol. 65, Iss. 2, pp. 434 – 443, 2019.